

# Investigation of Effect of Dynamic Stall and Its Alleviation on Helicopter Performance and Loads

Tin-Chee Wong, James A. O'Malley, III and David M. O'Brien, Jr.  
US Army Research Development and Engineering Command  
Aviation Engineering Directorate  
Redstone Arsenal, AL 35898

## Abstract

The static and dynamic stall characteristics of VR-7 baseline and two modified airfoils were computed and compared with available experimental data. The unsteady, compressible Reynolds-averaged Navier-Stokes equations based on an unstructured-grid approach with the one-equation Spalart-Allmaras turbulence model has been used to investigate flow over these airfoils in stationary and oscillating conditions. The baseline VR-7 results correlate well with static test data; the computed dynamic results of the VR-7 show a large negative pitching moment and drag observed in the hysteresis curves and agree fairly well with dynamic test data. An optimization technique was used to modify the upper surface of VR-7 airfoil with the cost function of minimized drag while maintaining a specified lift. The computed static and dynamic characteristics of the modified airfoils at low Mach numbers show improvement in the static characteristics and a large reduction of the negative pitching moment in the dynamic case. The effect on helicopter performance and loads are analyzed using a comprehensive analysis code with the computed static and dynamic characteristics of VR-7 and modified VR-7 airfoils for aerodynamics.

## Introduction

The dynamic stall phenomenon has been known to be a major factor that limits helicopter rotor performance at high forward speed flight, in high normal load factor maneuvers, and at high density-altitude because of the onset of large airloads and vibration. Stall occurs on a helicopter rotor at relatively high airspeed as the advancing and retreating blades begin to operate close to the attached flow limits. These limits are a direct result of the blade flapping and large pitching moments that characterize the performance of an airfoil operating through dynamic stall. Recent desert and mountainous region operations have challenged current helicopters with the requirement to operate effectively in high density-altitude conditions. Relieving the limitation due to dynamic pitching moment stall through the use of an advanced airfoil such as VR-12, a control nose-droop concept [1] or a passive control device by means of a miniature leading edge vortex generator [2] may provide useful increased rotor limits. However, the motivation of the present work is to analyze numerically both static and dynamic stall characteristics of VR-7 advanced airfoil and seek a low-cost method to alleviate the dynamic stall on the retreating blade without compromising the

advancing blade performance. An adjoint optimization coupled with an unstructured Navier-Stokes flow solver (FUN2D) was successfully applied to a multi-element RC-8 advanced airfoil to reduce drag of the main airfoil by optimizing the slat orientation [3]. In this work, the same technique is applied to the VR-7 airfoil to change upper surface of the airfoil to obtain better static characteristics and enable alleviation of the dynamic pitching moment divergence.

## Governing Equations

The unsteady, compressible Reynolds averaged Navier-Stokes equations written in Cartesian coordinates  $(x_1, x_2, x_3)$  for a moving control volume in integral form is given by

$$\frac{\partial}{\partial t} \int_V \bar{q} dV + \int_{\partial V} (\bar{F}_j - \bar{F}_{v,j}) \cdot \hat{n} dS = 0; \quad j=1, 2, 3$$

where  $V$  is the control volume, bounded by control surface  $\partial V$  with local face speed  $|W|$ . For the case of stationary control volume,  $|W|$  is zero. The vector  $\bar{q}$  represents the conserved variables which is defined as

$$\bar{q} = \begin{bmatrix} \rho \\ \rho u_1 \\ \rho u_2 \\ \rho u_3 \\ E \end{bmatrix}$$

---

*Presented at the American Helicopter Society 62<sup>nd</sup> Annual Forum, Phoenix, Arizona, May 9-11, 2006. This paper is declared a work of the United States Government and is not subject to copyright protection in the United States.*

the inviscid vector  $\vec{F}_j$  is

$$\vec{F}_j = \begin{bmatrix} \rho(u_j - W_j) \\ \rho u_1(u_j - W_j) + p \\ \rho u_2(u_j - W_j) \\ \rho u_3(u_j - W_j) \\ (E + p)(u_j - W_j) + W_j p \end{bmatrix} \vec{e}_j ; j=1, 2, 3$$

and the viscous vector  $\vec{F}_{vj}$  is

$$\vec{F}_{vj} = \begin{bmatrix} 0 \\ \tau_{j1} \\ \tau_{j2} \\ \tau_{j3} \\ u_k \tau_{jk} + \frac{M_\infty}{(\gamma - 1) \text{Re}} \left( \frac{\mu}{\text{Pr}} + \frac{\mu_t}{\text{Pr}_t} \right) \frac{\partial T}{\partial x_j} \end{bmatrix} \vec{e}_j ; j=1, 2, 3$$

The  $u_1, u_2, u_3$  and  $e_1, e_2, e_3$  are the Cartesian velocity components and unit vectors in  $x_1, x_2, x_3$  direction, respectively. The  $\tau$ 's represent the Cartesian components of shear-stress tensor for a Newtonian fluid with Stokes hypothesis assumption. For convenience, all the tensors are expressed in indicial notation by

$$\tau_{jl} = \frac{(\mu + \mu_t) M_\infty}{\text{Re}} \left( \frac{\partial u_j}{\partial x_l} + \frac{\partial u_l}{\partial x_j} - \frac{2}{3} \delta_{jl} \frac{\partial u_k}{\partial x_k} \right) ;$$

$j, l=1, 2, 3$

where  $j$  and  $l$  are free indices and  $k$  is the summation index. The  $\delta_{jl}$  is the Kronecker delta function ( $\delta_{jl} = 1$ , if  $i=j$ ;  $\delta_{jl} = 0$ , if  $i \neq j$ ). The laminar viscosity,  $\mu$  is evaluated by using Sutherland's law

$$\mu = \frac{1 + C}{T + C} T^{\frac{3}{2}}$$

Where  $T$  is the temperature and  $C = 198.6 / \tilde{T}_\infty$  ( $C$  denotes a dimensional quantity). The turbulent eddy viscosity,  $\mu_t$  is determined through turbulence model. The Prandtl number,  $\text{Pr}$  and turbulent Prandtl number,  $\text{Pr}_t$  are chosen to be 0.72 and 0.9, respectively. The static pressure,  $p$  is related to the total energy per unit volume,  $E$  for an ideal gas by the equation of state

$$p = (\gamma - 1) \left[ E - \frac{1}{2} \rho (u_1^2 + u_2^2 + u_3^2) \right]$$

The governing equations are made dimensionless using the free-stream density,  $\tilde{\rho}_\infty$ , speed of sound,  $\tilde{a}_\infty$ , molecular viscosity,  $\tilde{\mu}_\infty$ , dynamic pressure,  $\tilde{\rho}_\infty \tilde{a}_\infty^2$ , and a characteristic length,  $L$  such that the Reynolds number ( $\text{Re}$ ) and Mach number ( $M_\infty$ ) appear in the stress tensor and heat flux vector.

### Solution Algorithm

The unstructured mesh flow solver used in this study is FUN3D. This flow solver has been developed and supported by the NASA Langley Research Center and the detail of the numerical approach can be found in [4, 5, 6]. The code uses an implicit, upwind, finite-volume discretization in which the dependent variables are stored as mesh vertices. Inviscid fluxes at cell interfaces are computed using the flux-differencing scheme of Roe [7] and viscous fluxes are evaluated by using an approach equivalent to a central-difference Galerkin procedure. For steady-state flows, temporal discretization is performed by using a backward Euler time-stepping scheme. At each time step, the linear system of equations is approximately solved with an implicit line relaxation scheme [5]. A local time-step technique is employed to accelerate convergence to steady-state solution. For the time-accurate pitching oscillation, a generalized backward difference scheme (BDF) is used to construct a higher order temporal scheme by extending the difference stencil in time [6]. Within the nonlinear iteration process between time steps, the governing equations are advanced in pseudo time with local time stepping to accelerate the solution to a steady state in pseudo time, with the physical time step being constant over the entire mesh. The first-, second-, and third-order accuracy in time can be obtained using this BDF scheme. A temporal error control method is implemented as an exit criterion for the sub-iterative loop of the dual time stepping process. The details of the mesh movement, BDF and temporal error control schemes can be found in reference 6. For all unsteady pitching cases presented in this paper, the solution is second order accurate in time and space and the specified fraction of temporal error control is 0.1. All results presented in this paper, the one-equation model of Spalart and Allmaras is employed and solved in a loosely coupled fashion. The two-dimensional version of FUN3D has been extensively used to analyze airfoil characteristics for rotorcraft applications [8].

An adjoint optimization method coupled with the two-dimensional unstructured Navier-Stokes solver (FUN2D) is also applied to the VR-7 baseline airfoil

section in order to obtain two new airfoil profiles. The optimization method allows the modification of an airfoil shape based on a set of cost functions while maintaining a set of constraints. The cost function of the present study consists of lift and drag coefficients and the constraints are the limits placed on the airfoil deformation. During the optimization process, the mesh is continuously updated as the shape of airfoil changes. The optimization tool uses a discrete adjoint formulation to obtain sensitivity derivatives due to the movement of interior mesh points on unstructured grids. The optimization algorithm, KSOPT [9] along with a mesh movement method coupled with the flow solver including a fully coupled Spalart and Allmaras turbulence model were packaged and distributed by the NASA Langley Research Center [4]. It is not the scope of this paper to explain the details of this method, but to show the application of these tools for rotorcraft application.

## Results and Discussion

Computations were performed at two Mach numbers of 0.3 ( $Re=4 \times 10^6$ ) and 0.4 ( $Re=5 \times 10^6$ ) at a single reduced frequency of 0.1. These conditions are representative of a typical retreating blade stall condition. All meshes used in this study were generated using the AFLR grid generator developed by Mississippi State University [10]. The airfoil chosen for this study is the VR-7 airfoil with a trailing-edge reflex of three degrees for comparison with data of [11]. Figure 1 shows a typical two-dimensional unstructured mesh for a VR-7 airfoil section. The extent of the computational domain is 20 chords away from the center of the airfoil with off-surface spacing of  $10^{-6}$  chord length yielding a  $y^+$  of one. For the present calculations, the flow was assumed to be fully turbulent. All dynamic stall cases were started with a converged steady-state solution at  $\alpha = 10^\circ$ , such that only three periods were required to obtain sufficient periodic convergence.

### Dynamic Stall Validation Case

The VR-7 airfoil and the flow and motion conditions were chosen to represent the tunnel test case of 45117 in Reference 11. The airfoil is pitched in a sinusoidal motion about the quarter chord, according to

$$\alpha = \alpha_m + \alpha_o \sin(2kM_\infty t)$$

where  $\alpha$  is the instantaneous angle of attack,  $\alpha_m$  is the mean angle of attack,  $\alpha_o$  is the pitch amplitude and  $k$  is the reduced frequency. This dynamic stall case of freestream Mach number of 0.3 is defined by the parameter set  $\alpha_m = 10^\circ$ ,  $\alpha_o = 10^\circ$  and  $k = 0.1$ . Four grids were generated to investigate grid refinement effect on

the dynamic characteristics of the baseline VR-7 airfoil section. The original mesh (Grid 3) contained 123,814 nodes with 621 points around the airfoil and 201 points distributed over the outer boundary. Three sources were placed behind the blunted trailing edge of the airfoil to cluster grid points at the wake region. To evaluate the effect of grid refinement, this fine mesh was also coarsened successively with a factor of 2 in both surface and outer boundary points generating meshes of 39,499 (Grid 2), and 14,550 (Grid 1) nodes. The finest mesh (Grid 4) of 132,184 nodes is also created with surface point increases about 20% of Grid 3. For this deep stall pitching simulation, FUN3D was run in two-dimensional mode (two parallel planes with span of 2) and each mesh was computed using time step of 3000 steps per cycle. Figure 2 shows the effect of grid refinement on the lift variation. All the meshes under-predict the lift slope during the upstroke but the finer meshes (Grid 3 and Grid 4) show less discrepancy between computation and experiment (black) as the airfoil is pitching down. Figures 3 and 4 show the corresponding results of drag and pitching moment coefficients, respectively. The computed results correlate qualitatively well with the experimental data. The finer meshes (Grid 3 and Grid 4) improve the prediction close to the pitching moment stall, but the drag and pitching moment are over-predicted. It may be due to the one-equation turbulence model not being adequate for this highly separated flow. In general, the change in lift, drag and pitching moment coefficients obtained from Grid 3 (blue) and Grid 4 (orange) is minimal. Thus, Grid 3 is chosen for the next time-step refinement study. A snapshot of pressure contours during the upstroke for the  $M_\infty = 0.3$  case is shown in Figure 5. The pressure contours indicates the suction pressure reaching to a critical value at around  $\alpha = 19^\circ$  and adverse pressure gradients build up near airfoil leading edge. As the angle of attack increases to  $19.7^\circ$ , the low pressure originates from the trailing edge moves forward. As a result of trailing edge separation accompanied by the formation of shedding vortex from the leading edge, the low pressure wave moves downstream with increasing angle of attack. The vortex convection is marked by the pressure contours at  $\alpha = 19.9^\circ$  in Figure 5. This sequence of events creates the double peaks in the lift coefficients prior to dynamic stall.

Four cases were computed on Grid 3 with time step increment of 1000 step per cycle. Figure 6 shows the time-step refinement on computed lift coefficient along with the experimental data. There is more variation in the computation as the time step is refined from 1000 to 2000 steps per cycle, especially the

airfoil is pitched down and the shed vortex travels over the upper surface of the airfoil. Similar trend has observed from the corresponding results in Figures 7 and 8. More variation in the computation is observed as the airfoil pitched down than the pitched up region. Even though the computed results on the finest mesh with the smallest time step do not replicate the experimental data, the change in three coefficients becomes smaller with decreasing time step. It indicates that the solution essentially converged for this mesh. The time step of 3000 steps per cycle on Grid 3 is considered reasonable and chosen for the current study. For each complete cycle, it requires 89 CPU hours with 32 processors and 174 CPU hours with 24 processors on an SGI Altix Linux and Origin 3900 machines, respectively.

### Static Validation Case

Steady-state cases of flow over the baseline VR-7, and two modified airfoil sections at a free-stream Mach number of 0.3 and a Reynolds number of 4 million were computed using a pseudo-time stepping scheme over a range of angles of attack between  $-5^\circ$  and  $20^\circ$ . Two modified profiles of the baseline VR-7 airfoil were obtained using the adjoint optimization method for Mach numbers of 0.3 (Opt  $\alpha = 10^\circ M_\infty = 0.3$ ) and 0.4 (Opt  $\alpha = 10^\circ M_\infty = 0.4$ ) respectively, at  $\alpha = 10^\circ$ . The objective is to reduce the drag coefficient while maintaining specified lift. The cost function,  $I_c$  is defined as a linear combination of the lift and drag coefficient

$$I_c = 25C_d^2 + (C_l - C_{l\_target})^2$$

where  $C_{l\_target}$  is the target lift coefficient of 1.5 and the target drag coefficient is zero in this case. The drag is weighted more heavily than the lift such that both contributions are approximately equal [4]. Moreover, eight y-coordinate limits are chosen as design variables to constrain movement of control points only on the upper surface of the airfoil up to 35% of the chord length during the optimization.

After 25 design cycles, the drag has been reduced from 0.0274 to 0.0238 and the lift has increased from 1.348 to 1.373 for  $M_\infty = 0.3$ . For the case of Mach number of 0.4 drag has reduced from 0.0259 to 0.0243 while the lift remains unchanged. It is noticed that both cases, the nose-down moment is slightly reduced. Figure 9 shows a comparison of the original (red) and two airfoil profiles optimized at  $M_\infty = 0.3$  (green) and  $M_\infty = 0.4$  (blue). Each case took 43.5 CPU hours for 25 design cycles on an Origin 3900 machine using 24 processors.

The static lift, drag and pitching moment coefficients for the original VR-7 and two optimized airfoils are presented in Figures 10-12. The computed lift coefficient of original VR-7 profile (red) compared fairly well with the experimental data (square symbol). Both modified profiles increase the maximum lift coefficient ( $C_{l\_max}$ ) and have better post-stall characteristics (Figure 10). The computed drag and pitching moment coefficient of original airfoil show larger discrepancy as compared with experiment for  $\alpha > 13^\circ$ . The drag of both modified airfoil has slightly less as compared with the original one for  $\alpha > 7^\circ$ . The two optimized airfoils have slightly higher nose-down moment beyond static stall as compared with the original airfoil (Figure 12). Figure 13 show the comparison of surface-pressure coefficient with experimental data at angle of attacks in the static stall region. The computed pressure coefficient compares very well with the experiment.

Three steady-state cases were re-computed with Mach number of 0.4 and Reynolds number of 5 million for the same airfoils. Figures 14-16 show the comparison of lift, drag and pitching moment coefficients for the original, and two modified airfoils. The optimized airfoil profile at Mach number of 0.4 indicates higher  $C_{l\_max}$  and has better post-stall characteristics at operating condition of  $M_\infty = 0.4$ .

### Dynamic Case of Modified Airfoils

#### Results for $M_\infty=0.3$

The validation case of sinusoidal pitched airfoil previously presented was re-computed with these two optimized airfoils at Mach number of 0.3 to investigate the impact of dynamic stall characteristics due to the minor change in airfoil profile. Figures 17-19 show a comparison of lift, drag and pitching moment coefficients between the original VR-7 and the two optimized airfoils. The original airfoil shows a large nose-down moment and a corresponding drag rise at the angle of attack of dynamic moment stall. The two modified airfoils result in a large reduction of the nose-down moment divergence at the dynamic stall condition. A snapshot of pressure contours of the modified airfoil (Opt  $\alpha = 10^\circ M_\infty = 0.3$ ) is shown in Figure 19. It is noticed that the level of the suction peak around the leading edge is lower than the one from the baseline airfoil (Figure 5). Therefore, the signature of vortex convection above the modified airfoil is not as dominant as compared with the results from baseline airfoil (Figure 20). The magnitude of

the nose-down moment is reduced by 60%. The result of the modified airfoil that is optimized at Mach number 0.4 shows quite similar behavior.

### Results for $M_\infty=0.4$

Two cases of sinusoidal pitched airfoils were computed for two optimized airfoils at Mach number of 0.4 and Reynolds number of 5 million. The histories of lift, drag and pitching moment coefficients are shown in Figures 21-23. The modified airfoils have a higher lift slope as compared with the baseline airfoil, but the moment stall occurs slightly earlier. The Mach contour plot indicates that the mechanism causing the boundary-layer separation as Mach number increases from 0.3 to 0.4 is induced by the shock formed at the leading edge (upper left of Figure 24). A snapshot of the calculated pressure contour shows the footprint of shock and the formation of a stall vortex (lower right of Figure 24). Both modified airfoils do not alleviate the stall moment in this case. The failure of the adjoint optimization approach to give an appropriate profile based on the steady-state assumption in the design process is probably due to the fact that the shock induced separation does not appear in the static calculation.

### Helicopter Rotor Loads and Performance

Helicopter performance and comprehensive analysis codes utilize look-up tables to provide two dimensional aerodynamic characteristics. FUN2D was used to construct the baseline airfoil table and the two modified airfoil tables. The three coefficients ( $c_l$ ,  $c_d$ ,  $c_m$ ) were computed for 7 Mach numbers and 98 angles of attack ranging from  $-180^\circ$  to  $180^\circ$ . The increment of  $5^\circ$  is used everywhere except in the range between  $-5^\circ$  and  $25^\circ$  where  $1^\circ$  is used. The generation of each table required 675 CPU hours with 16 processors on a SGI Origin 3900 computer. The airfoil tables along with the dynamic stall characteristics are utilized as the blade section aerodynamics for the comprehensive analysis code C81 [12] to investigate the rotor system pitch-link loads and performance. C81 has two unsteady, dynamic stall methods available when the time variant trim option is used. The Bell Unsteady (BUNS) empirical model is based on the Carta method [13]. The Unsteady Analysis (UNSAN) empirical model is the Gormont-Harris method [14]. The UNSAN method has been modified to better represent the drag and moment results obtained by FUN3D and the comparison is shown in Figure 25 for the VR-7 airfoil. The method has been modified to better represent the predominant feature of the dynamic characteristic, i.e.

the magnitude of the drag and moment at the highest angle of attack.

The CH-47D tandem rotor helicopter has been modeled in C81 to provide an expeditious precursor to the more complicated second generation comprehensive models (such as 2GCHAS and the Rotorcraft Comprehensive Analysis System, RCAS). For example, C81 provides accurate trim information in a few seconds on a PC as indicated by the resultant small difference (0.4 deg) in helicopter pitch attitude shown in Figure 26. Four blade bending modes calculated by the Myklestad method [15] are used in C81 applied to each rotor to obtain the loading represented by Figure 27. The modes include two beam, one chord and one torsion bending. The ratio of the C81 calculated oscillatory torsional bending moment to the 2GCHAS calculation indicates much higher inboard loads but about the same for the outboard 30%. The C81 calculated oscillatory beam bending moment is taken as a ratio to the available test measured loads and indicates 20 to 40% higher calculated loads in the middle of the blade (where the test showed a constant loading). The calculated load results indicate that a comparative analysis using C81 can be conducted to show real differences.

To investigate the effects of incorporating the small modification to the baseline VR-7 required for the optimized section, C81 has been used to compute pitch link loads (PLL) for high Gross Weights at a density altitude of 7122 ft for level flight at 115 and 125 KTAS. The high Gross Weights represent up to about 1.25 g steady state turns based on the Hover Out of Ground Effect (HOGE) take off gross weight capability at 4000 ft / 95 deg F. The airfoil modification shown in Figure 9 is referred to as small because it may be possible to achieve this profile change through the use of an urethane erosion strip. Figures 28 and 29 show the ratio of the pitch link loads calculated by C81 for the helicopter with the small airfoil modification to those for the helicopter with the baseline VR-7 airfoil. The calculated load reduction is about 10% for the highest PLL and about 40% for the lowest PLL. This shows that a significant reduction in rotor loads at flight conditions that are not unusual can be realized by designing the airfoil section to have dynamic stall characteristics that minimize the drag and moment magnitude variation, but retain the lift augmentation.

The Lifting Surface Aerodynamics and Performance Analysis of Rotors in Axial Flight (LSAF) [16] method is used to determine the HOGE performance with the modified VR-7 optimized at  $M_\infty=0.3$  versus the baseline VR-7. LSAF with the FUN2D generated

baseline VR-7 characteristics produces good correlation with existing whirl tower tests up to  $CT=0.01$  where the calculated Figure of Merit is 0.005 less than the test value. The LSAF comparative analysis is summarized in Figure 30 which shows the variation in rotor lift difference as a function of rotor power required. At the rotor power available limit, the total (two rotors) lift difference due to use of the modified airfoil vs. the baseline VR-7 airfoil is -80 lb; this is equal to only about 0.17% of the HOGE Gross Weight capability at the 4000 ft / 95 deg F condition.

## Conclusions

Unsteady, compressible Reynolds-averaged Navier-Stokes equation based on unstructured-grid approach with one-equation of Spalart-Allmaras turbulence model has been used to investigate flow over these airfoils in stationary and oscillating conditions. The static characteristics of VR-7 baseline and compared fairly well with available experimental data. The computed baseline VR-7 dynamic results show a large negative pitching moment and drag observed in the hysteresis curves and agree fairly well with dynamic test data. An optimization technique was used to modify the upper surface of VR-7 airfoil at two Mach numbers with the cost function of minimized drag while maintaining a specified lift. The modified airfoils result in a large reduction of nose-down moment divergence in the stall condition as compared with the baseline VR-7 airfoil. The computed airfoil tables along with the dynamic stall characteristics were used as the blade section aerodynamics for the comprehensive analysis code C81 to investigate the rotor system pitch-link loads. The Unsteady Analysis empirical method can be modified to better represent the drag and moment results obtained from CFD. CFD can be used to produce accurate airfoil data for use in Comprehensive analysis methods. An adjoint optimization method coupled with the two-dimensional unstructured Navier-Stokes solver (FUN2D) can be used to design fixed helicopter airfoil sections with reduced dynamic stall effects for drag and moment but with favorable lift overshoot. A minor upper surface modification on the VR-7 airfoil results in reduced dynamic stall effects and provides significant pitch link load reduction based on C81 calculations for the helicopter at high Gross Weights and mild steady state turns. The modified airfoil has a small effect on HOGE lift capability at the installed power limit.

## Acknowledgment

The authors would like to thank Drs. Eric Nielsen and Robert Biedron of the NASA Langley Research

Center for providing technical support on FUN2D/3D. The computer resources of the Department of Defense Naval Oceanographic Office Major Shared Resource Center and Distributed Center of the US Army Space and Missile Defense Command Simulation Center are gratefully acknowledged.

## References

- [1] Martin, P. B., McAlister, K. W., Chandrasenkara, M. S., and Geissler, W., "Dynamic Stall Measurements and Computations for a VR-12 Airfoil with a Variable Droop Leading Edge," 59<sup>th</sup> AHS Annual Forum, Phoenix, Arizona, May 2003.
- [2] Geissler, W., Ditzz, G., and Mai, H., "Dynamic Stall and Its Passive Control Investigations on the OA209 Airfoil Section," 31<sup>st</sup> European Rotorcraft Forum, Firenze, Italy Sept. 2005.
- [3] Chaffin, S. M., "Application of Adjoint Optimization Method to Multi-element Rotorcraft Airfoils," AHS Vertical Lift Aircraft Design Conference, San Francisco, 2000.
- [4] Anderson, W. K., and Bonhaus, D. L., "An Implicit Upwind Algorithm for Computing Turbulent Flows on Unstructured Grids," *Computers and Fluids*, Vol. 23, No. 1. pp. 1-21, 1994.
- [5] Nielsen, E. J., Lu, J., Park, M. A., and Darmofal, D. L., "An Implicit Exact Dual Adjoint Solution Method for Turbulent Flows on Unstructured Grids," *Computers and Fluids*, Vol. 33, No. 9, pp. 1131-1155, November 2004.
- [6] Biedron, R. T., Vatsa, V. N., and Atkins, H. L., "Simulation of Unsteady Flows Using an Unstructured Navier-Stokes Solver on Moving and Stationary Grids," AIAA Paper 2005-5093, June 2005.
- [7] Roe, P. L., "Approximate Riemann Solvers, Parameter Vectors, and Difference Schemes," *Journal of Computational Physics*, Vol. 43, No. 2, pp. 357-372, 1981.
- [8] Smith, M. J., Potsdam, M., Wong, T-C, Baeder, J. D., and Phanse, S., "Evaluation of Computational Fluid Dynamics to Determine Two-Dimensional Airfoil Characteristics for Rotorcraft Applications," *Journal of American Helicopter Society*, Vol. 51, No. 1, pp. 70-79, January 2006.

[9] Wrenn, G. A., "An Indirect Method for Numerical for Numerical Optimization Using the Kresselmeier-Steinhauser Function," NASA CR 42200, March 1989.

[10] Marcum, D. L., "Generation of Unstructured Grids for Viscous Flow Applications," AIAA Paper 95-0212, 1995.

[11] McAlister, K. W., Pucci, S. L., McCrosky, W. J., and Carr, L. W., "An Experimental Study of Dynamic Stall on Advanced Airfoil Sections Volume. Pressure and Force Data," USAAVRADCOTR-82-A-8 (or NASA TM 84245), Sept. 1982.

[12] Van Gaasbeek, J. R., "Rotorcraft Flight Simulation Computer Program C81 with Datamap Interface", USAAVRADCOTR-80-D-38A, Oct. 1981

[13] Arcidiacono, P. J., Carta, F. O., Casellini, L. M., and Elman, H. L., "Investigation of Helicopter Control Loads Induced by Stall Flutter", Sikorsky Aircraft, USAAVLABS TR 70-2, Mar 1970

[14] Gormont, R. E., "A Mathematical Model of Unsteady Aerodynamics and Radial Flow for Application to Helicopter Rotors", USAAMRDL TR 72-67, May 1973

[15] Schlomach, R. C. and May, J., "Rotor Blade Natural Frequency Analysis for Complex Hub Configuration", USAAVSCOM TR-85-D-22, July 1989

[16] Kocurek, J. D., Berkowitz, L. F. and Harris, F. D., "Hover Performance Methodology at Bell Helicopter Textron", 36<sup>th</sup> Annual Forum of the American Helicopter Society, Washington, D.C., May 1980

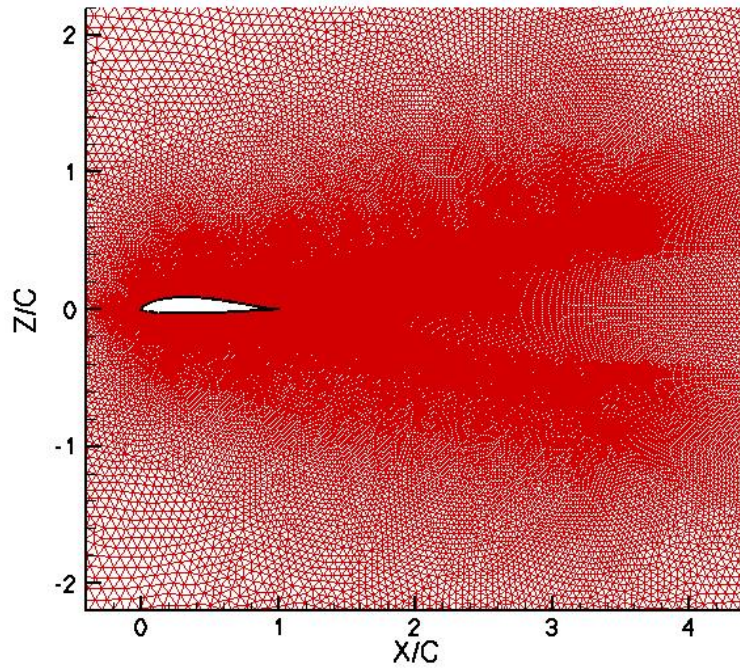


Figure 1 A typical unstructured mesh for VR-7 airfoil section.

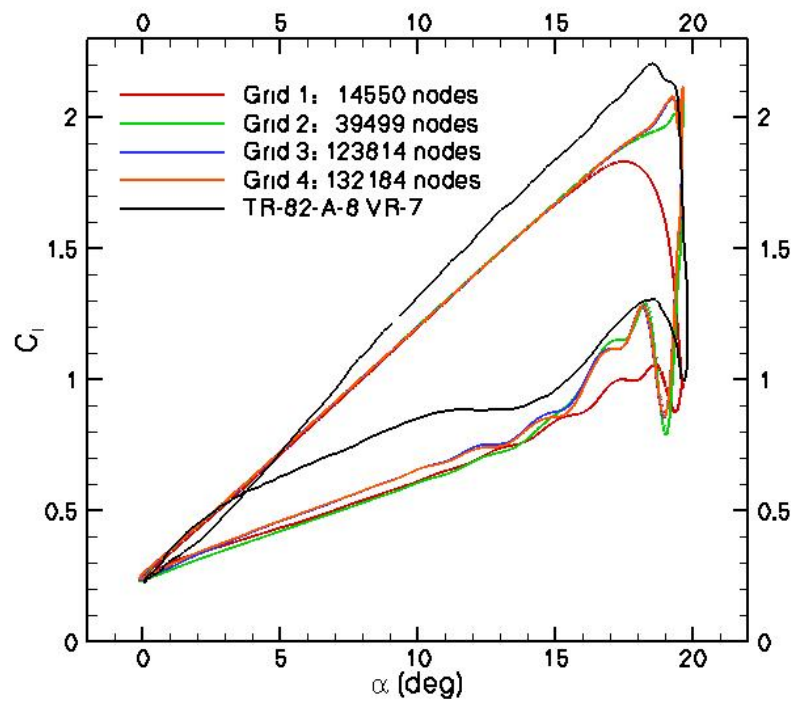


Figure 2 Effect of grid refinement on lift coefficient, baseline VR-7, experiment,  $M_\infty=0.3$ .

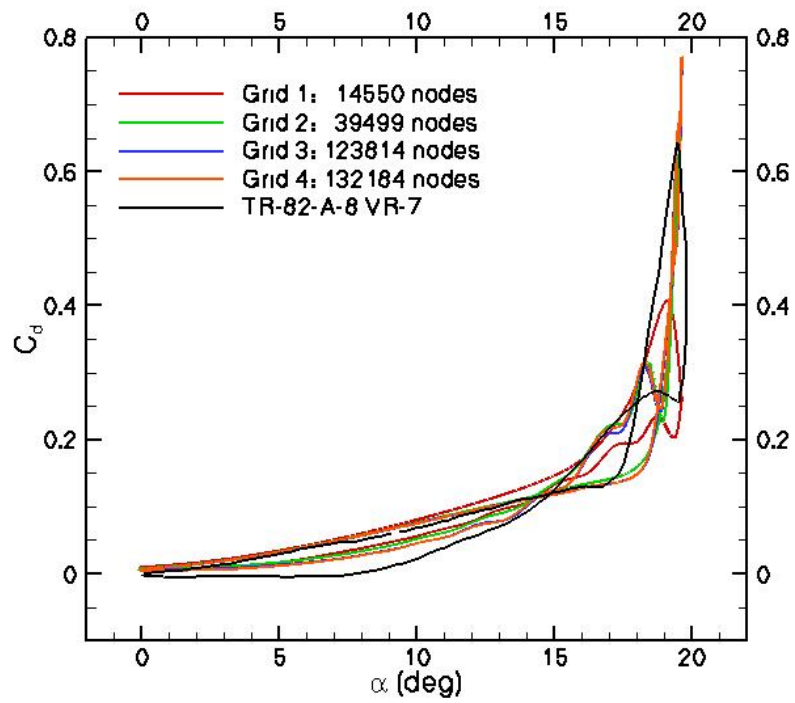


Figure 3 Effect of grid refinement on drag coefficient, baseline VR-7, experiment,  $M_\infty=0.3$ .

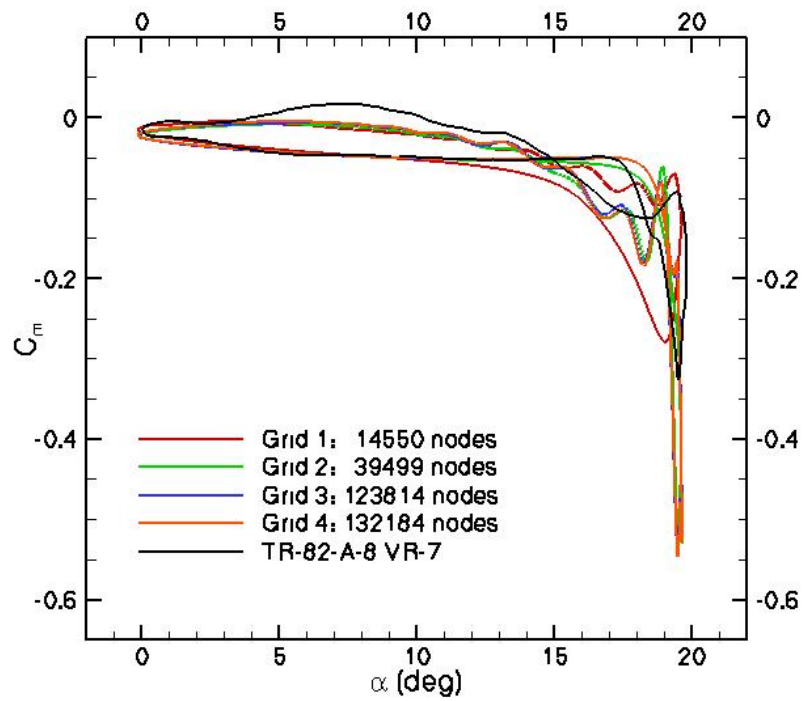


Figure 4 Effect of grid refinement on pitching moment coefficient, baseline VR-7, experiment,  $M_\infty=0.3$ .

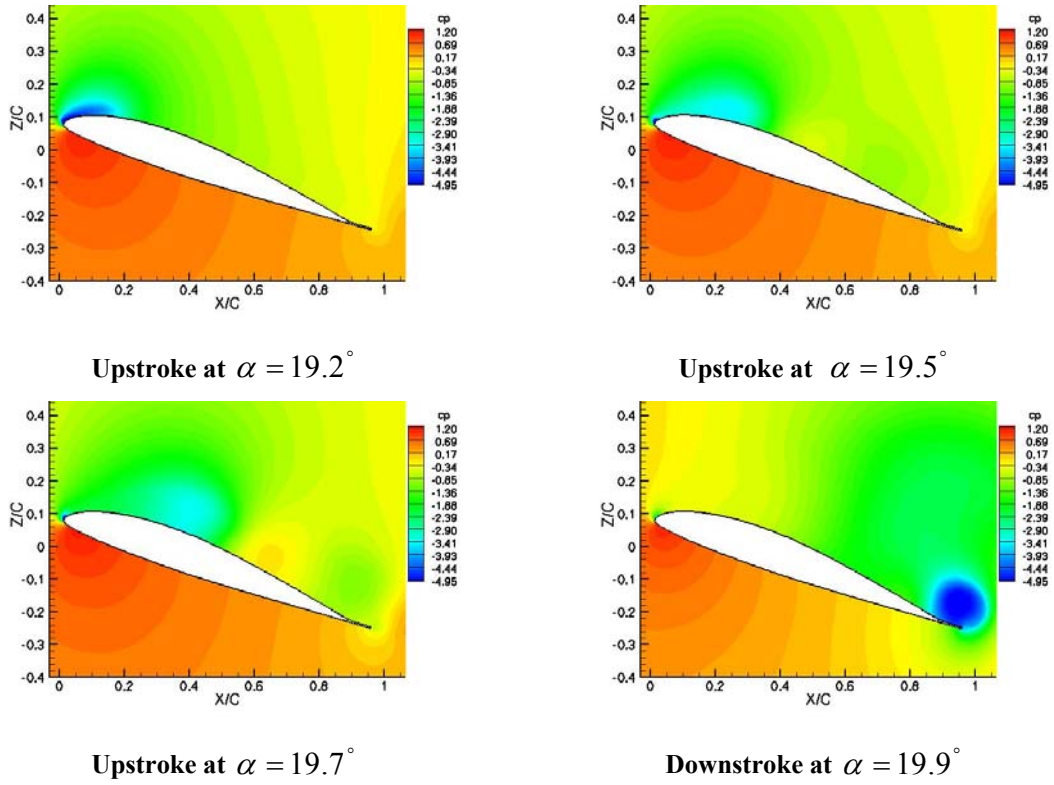


Figure 5 Pressure contours for VR-7 airfoil at  $M_\infty=0.3$  during pitching oscillation.

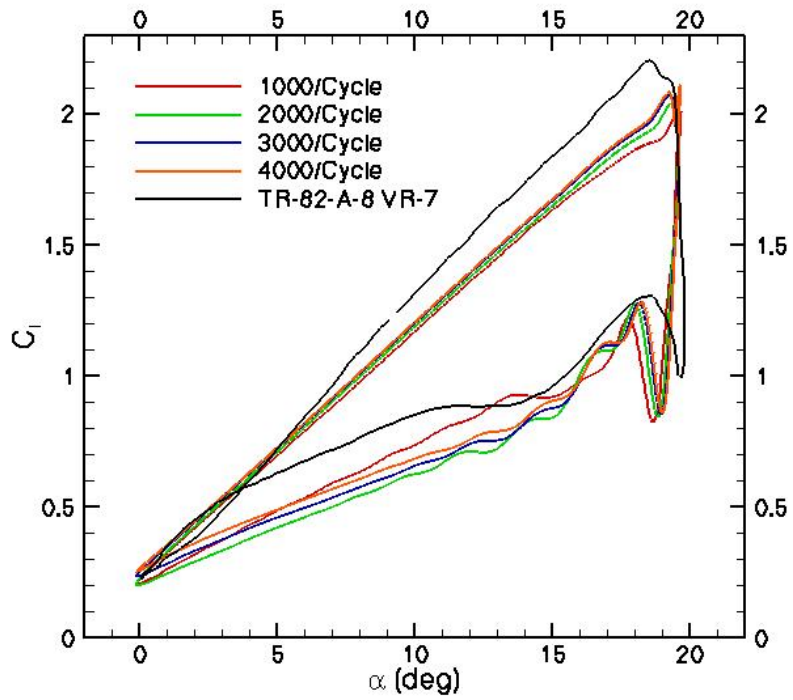


Figure 6 Effect of time-step refinement on lift coefficient, baseline VR-7, experiment,  $M_\infty=0.3$ .

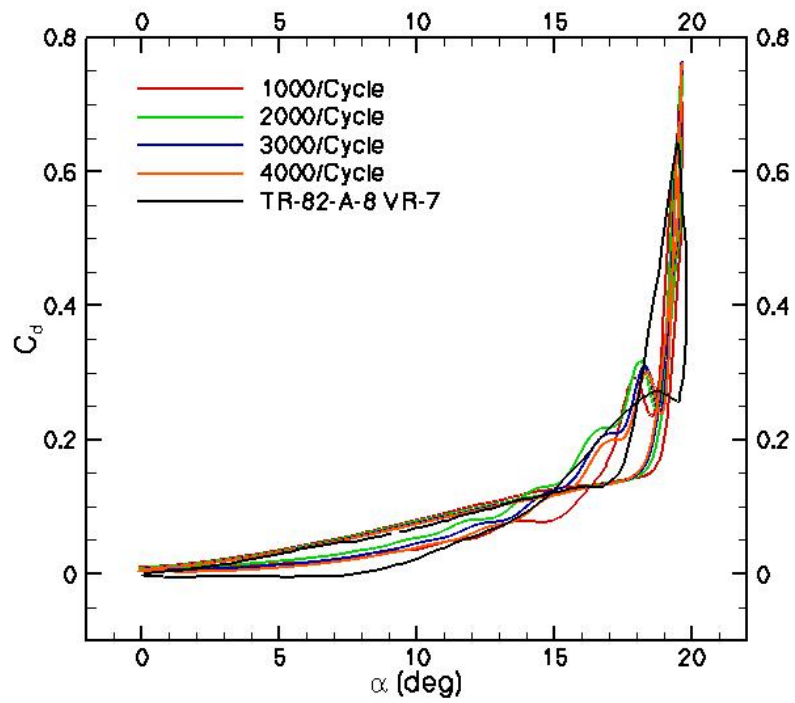


Figure 7 Effect of time-step refinement on drag coefficient, baseline VR-7, experiment,  $M_\infty=0.3$ .

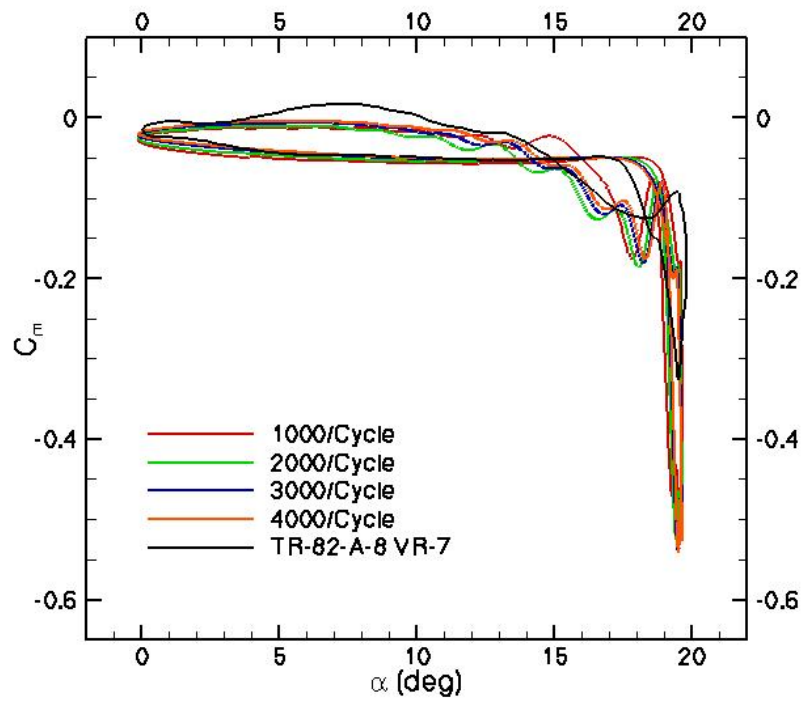


Figure 8 Effect of time-step refinement on pitching moment coefficient, baseline VR-7, experiment,  $M_\infty=0.3$ .

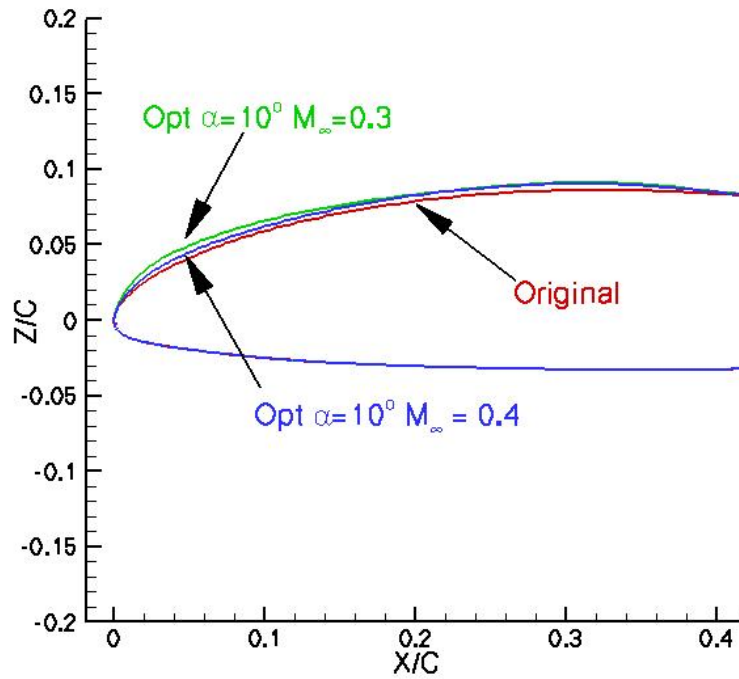


Figure 9 Comparison of baseline VR-7 with two modified airfoil profiles.

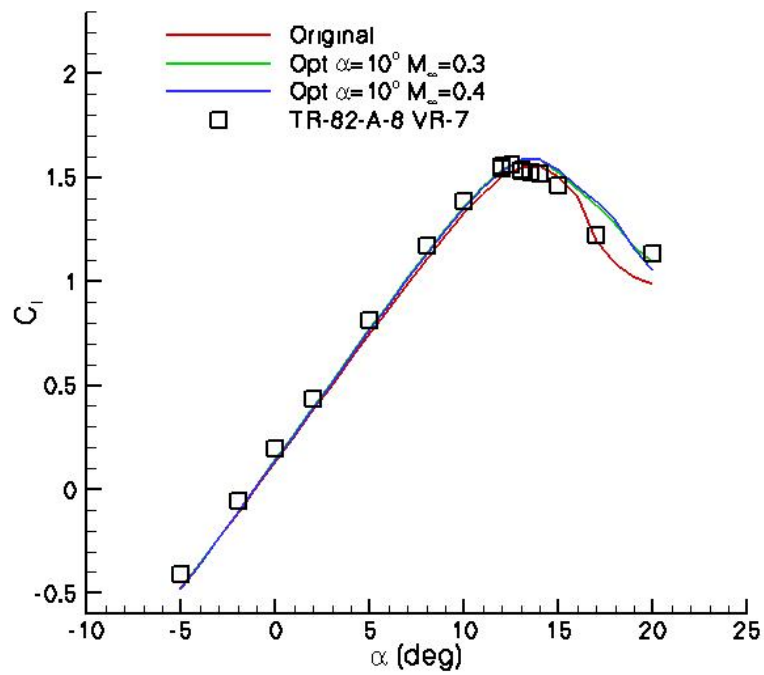


Figure 10 Comparison of lift coefficient of original VR-7, and modified airfoils with experiment at  $M_\infty=0.3$ .

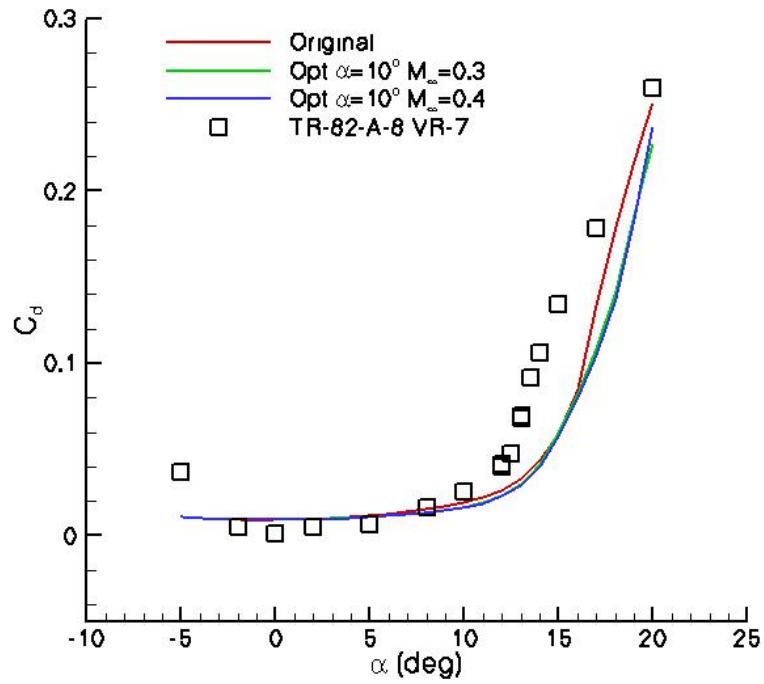


Figure 11 Comparison of drag coefficient for original VR-7, and modified airfoils with experiment at  $M_\infty=0.3$ .

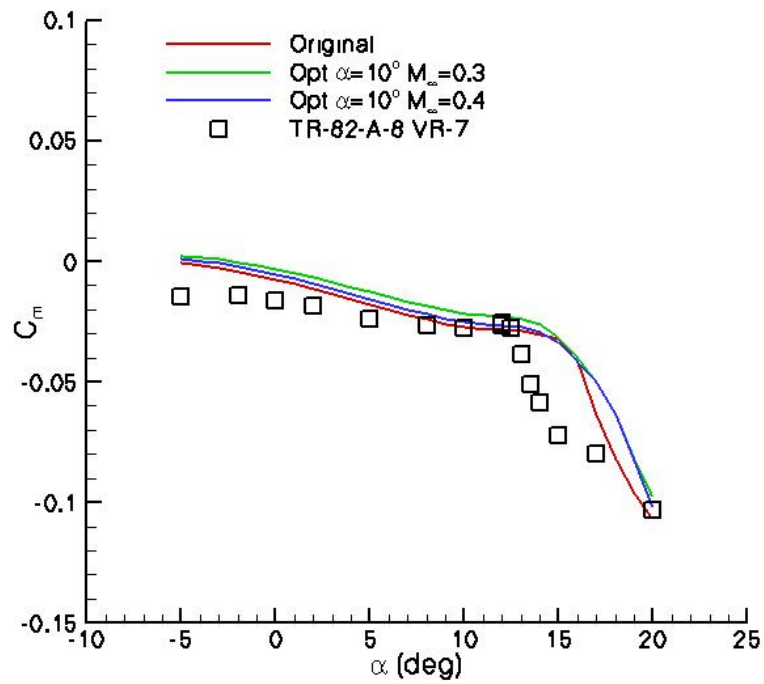


Figure 12 Comparison of pitching moment coefficient for original VR-7, and modified airfoil with experiment at  $M_\infty=0.3$ .

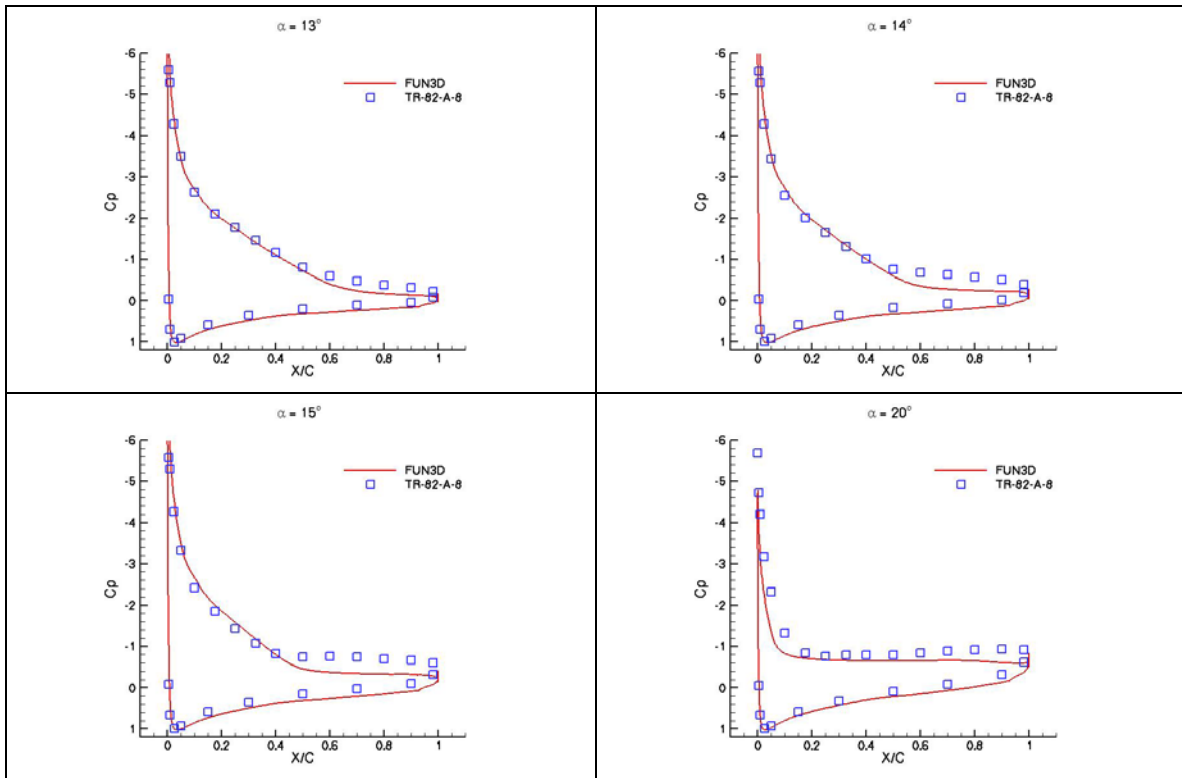


Figure 13 Comparison of surface-pressure coefficient of VR-7 airfoil with experiment at  $M_\infty=0.3$ .

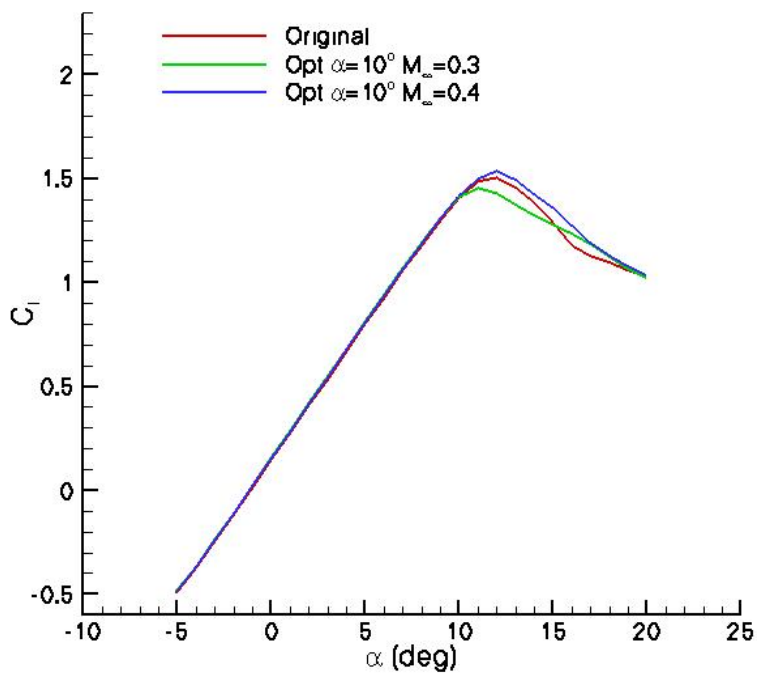


Figure 14 Lift coefficient of baseline VR-7 and two modified airfoils at  $M_\infty=0.4$ .

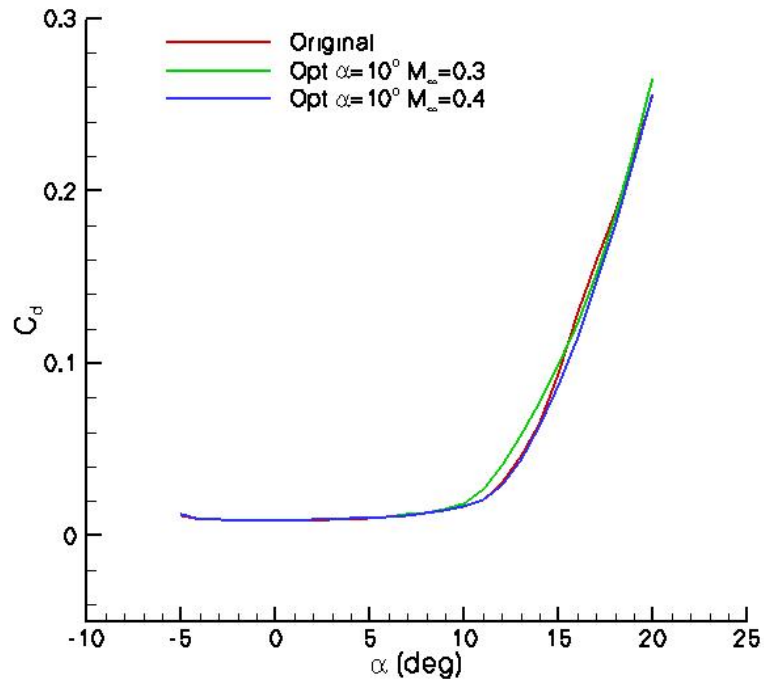


Figure 15 Drag coefficient of original VR-7 and two modified airfoils at  $M_\infty=0.4$ .

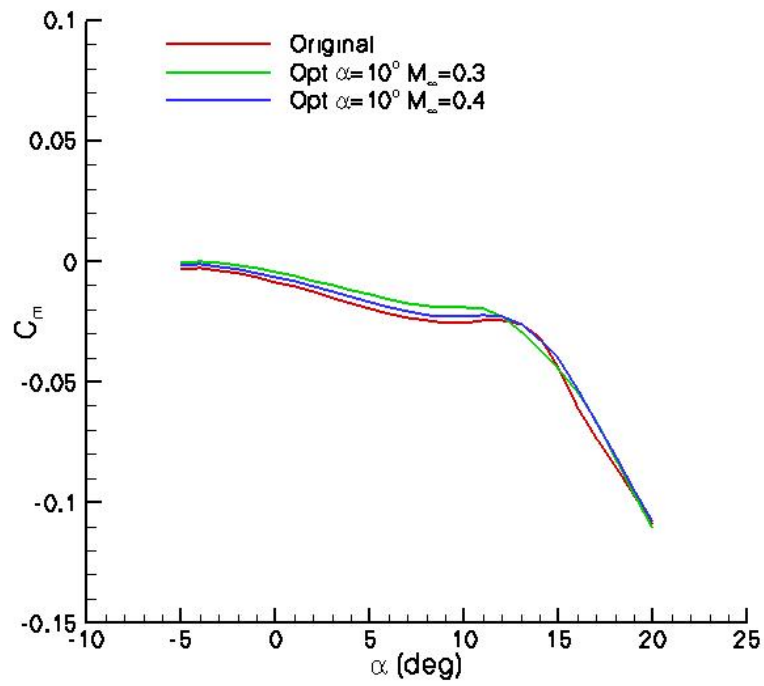


Figure 16 Pitching moment coefficient of original VR-7 and two modified airfoils at  $M_\infty=0.4$ .

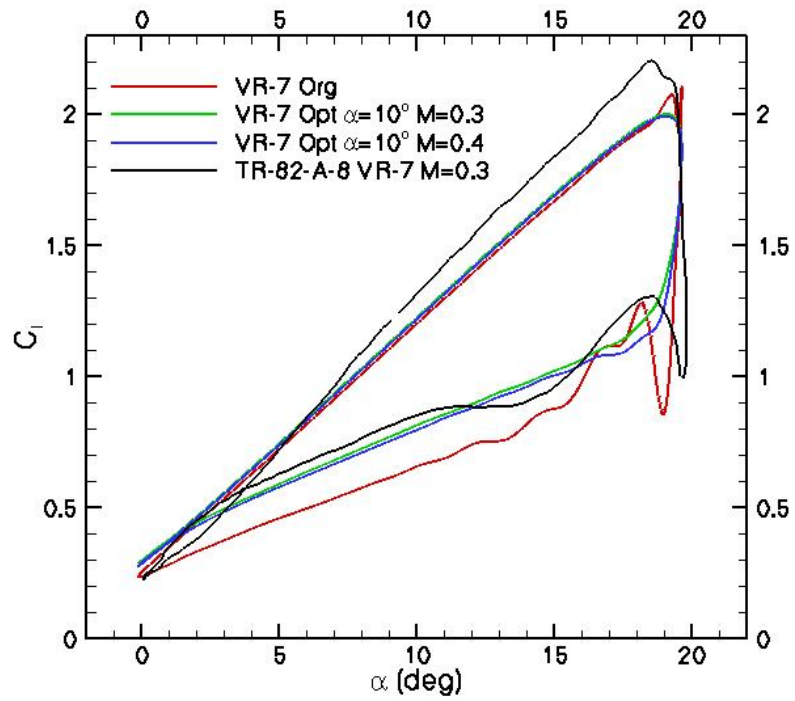


Figure 17 Hysteresis of lift coefficient of original VR-7, two modified airfoils and experiment at  $M_\infty=0.3$ .

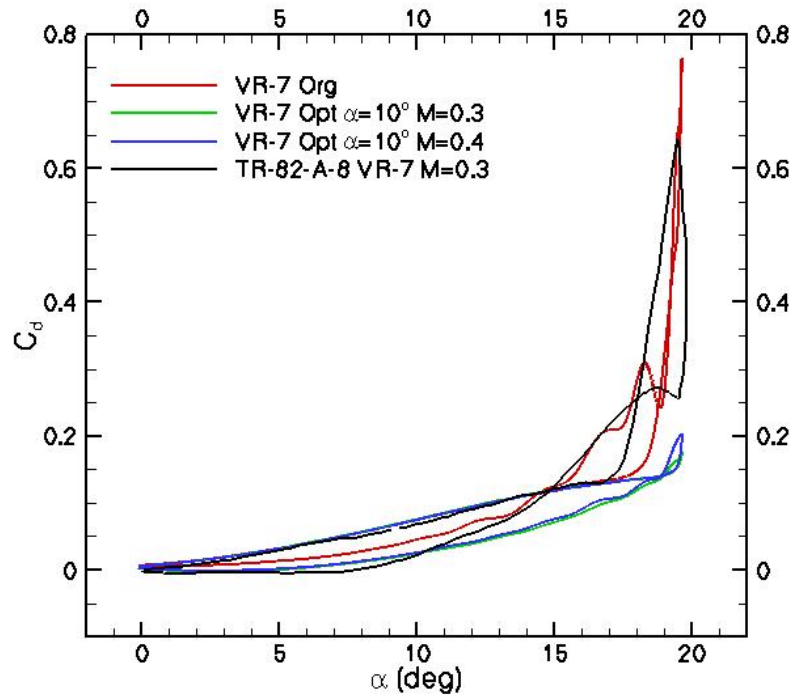


Figure 18 Hysteresis of drag coefficient of original VR-7, two modified airfoils and experiment at  $M_\infty=0.3$ .

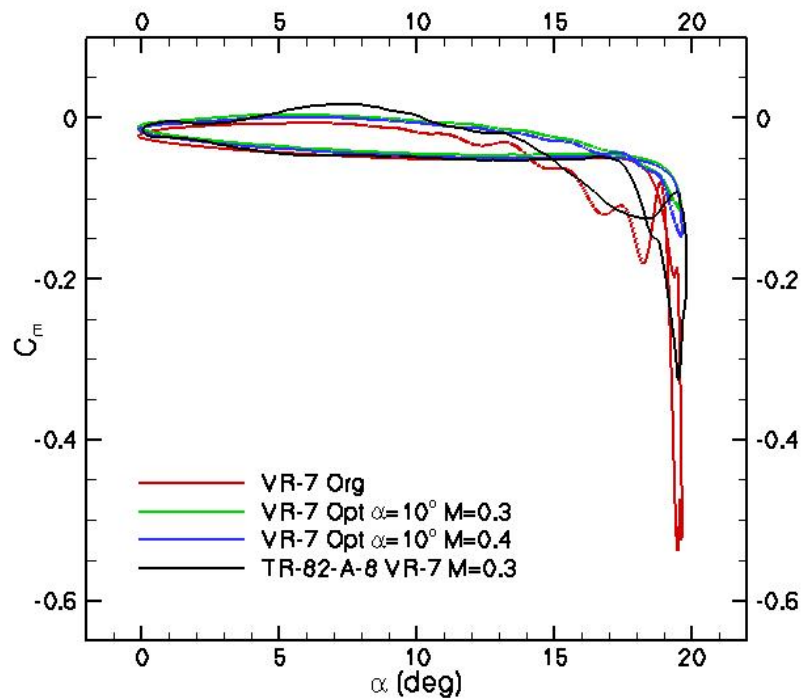


Figure 19 Hysteresis of pitching moment coefficient of VR-7, two modified airfoils and experiment at  $M_\infty=0.3$ .

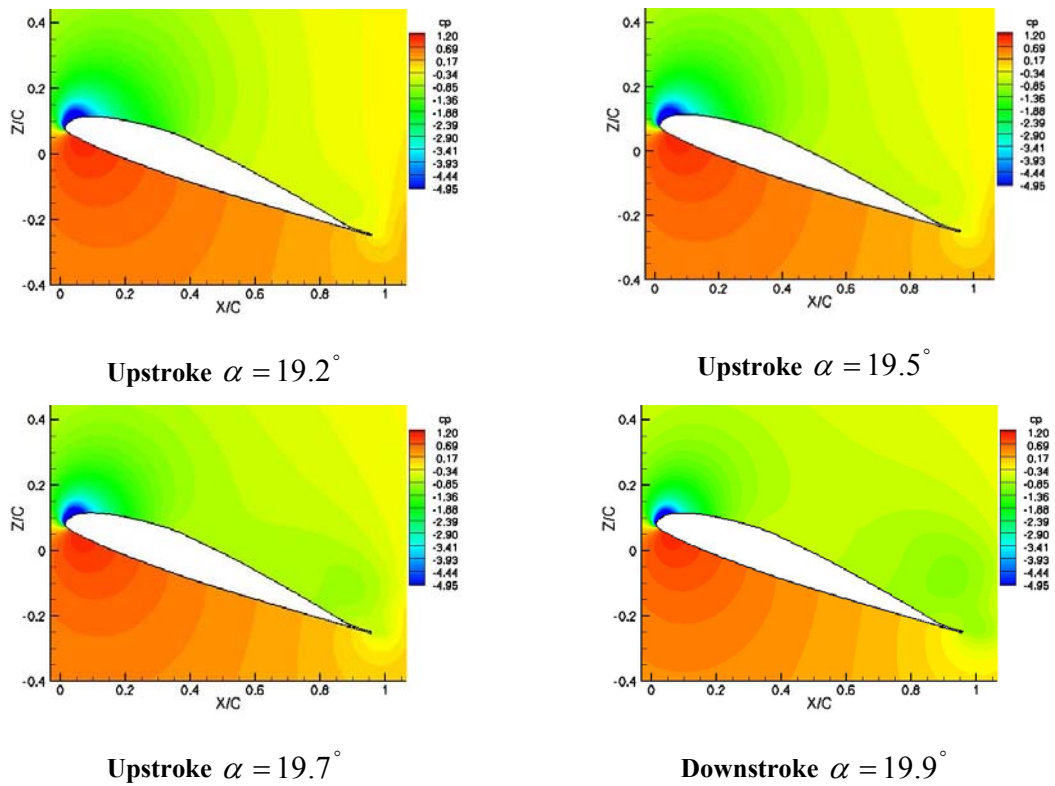


Figure 20 Pressure contours of modified airfoil at  $M_\infty=0.3$  during pitching oscillation.

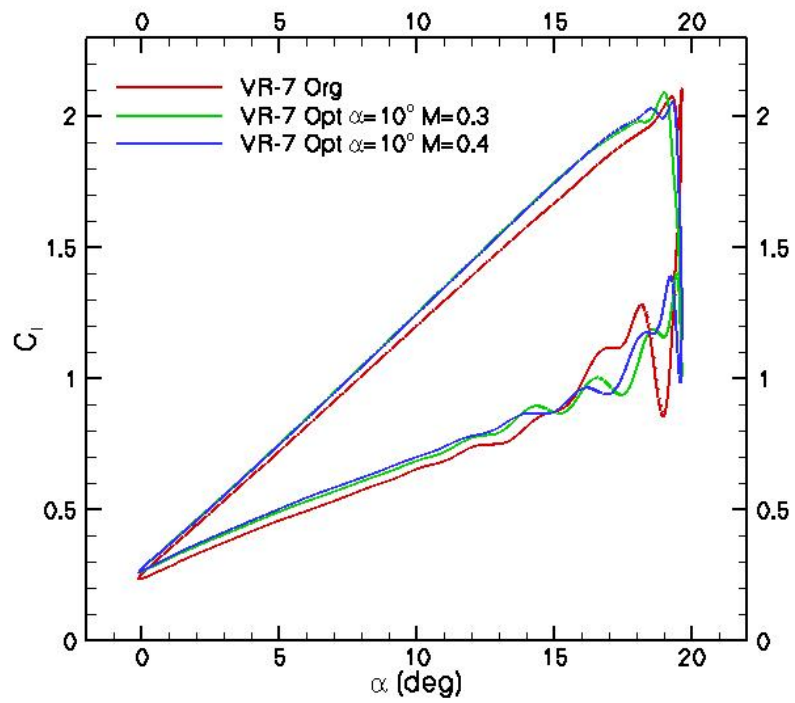


Figure 21 Hysteresis of lift coefficient of original VR-7 and two modified airfoils at  $M_\infty = 0.4$ .

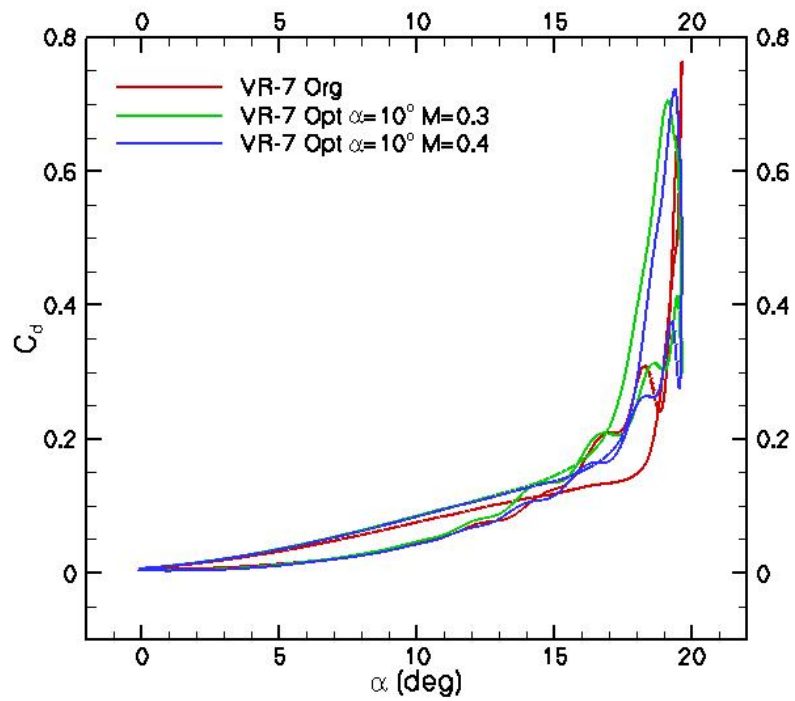


Figure 22 Hysteresis of drag coefficient of original VR-7 and two modified airfoils at  $M_\infty = 0.4$ .

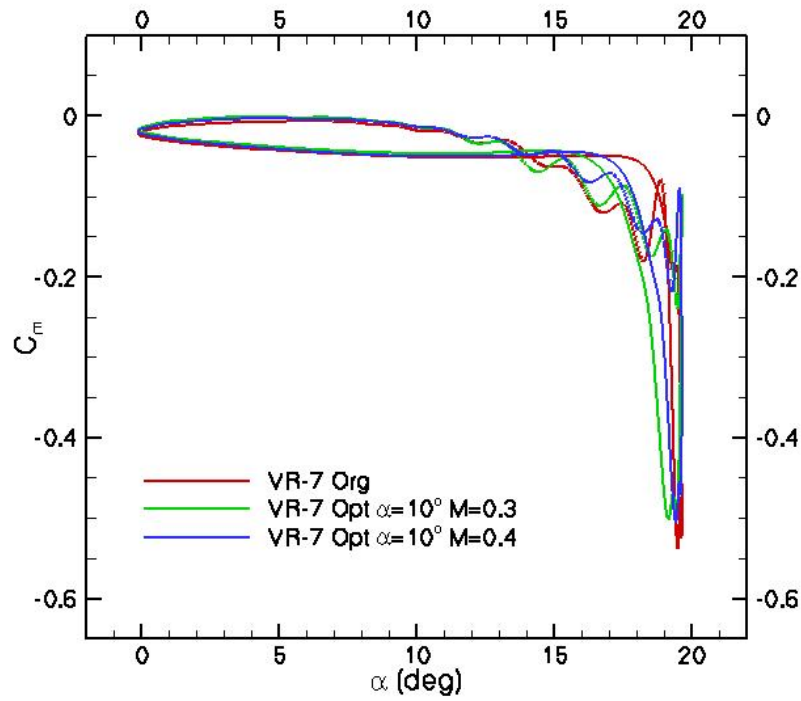


Figure 23 Hysteresis of pitching moment coefficient of original VR-7 and two modified airfoils at  $M_\infty=0.4$ .

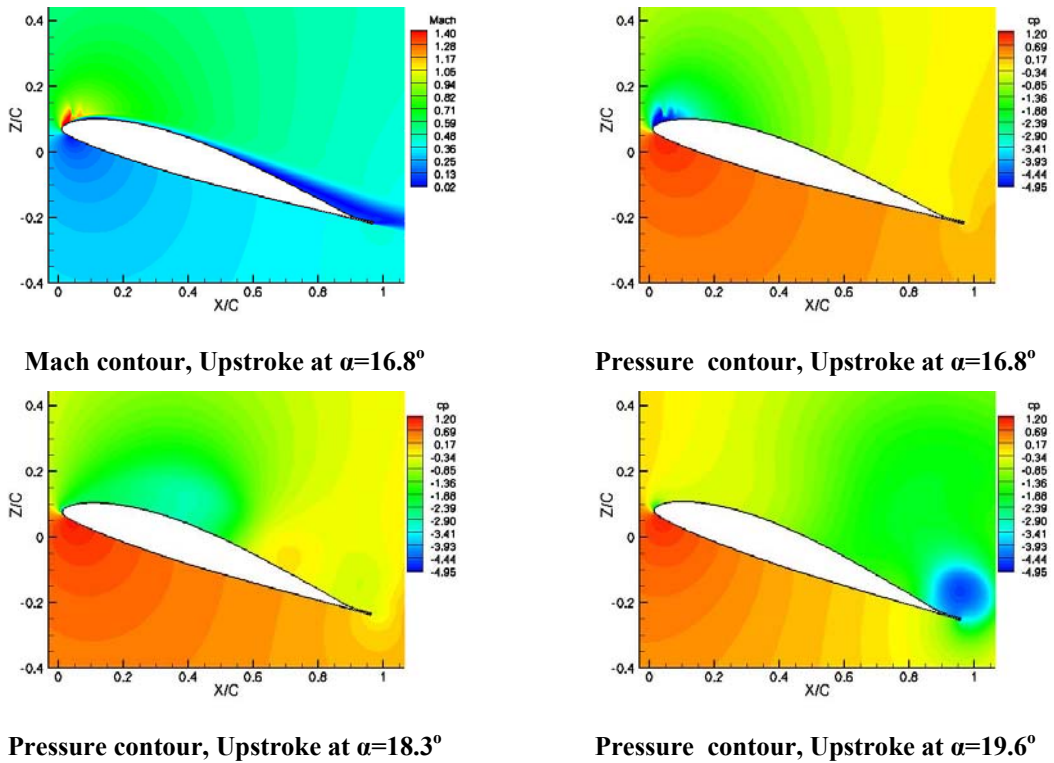


Figure 24 Snapshot of flowfield for baseline airfoil at  $M_\infty=0.4$  during pitching oscillation.

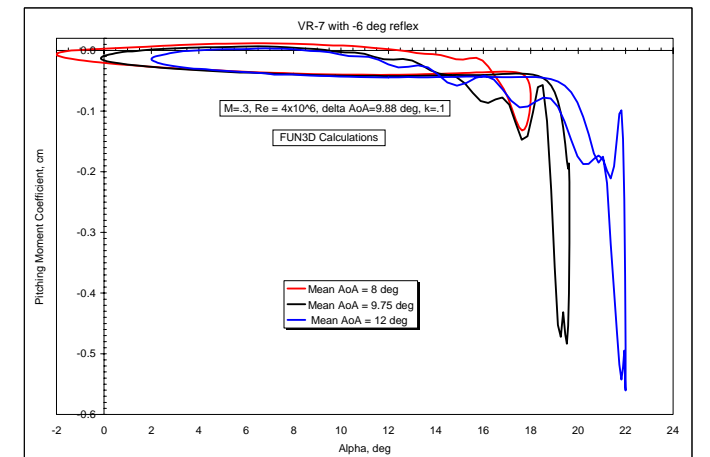
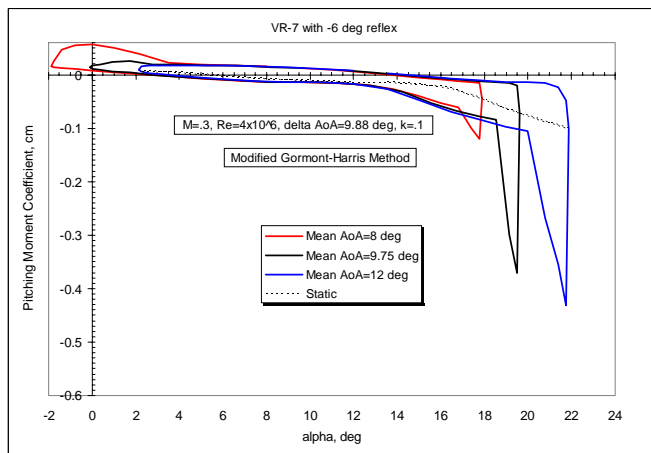
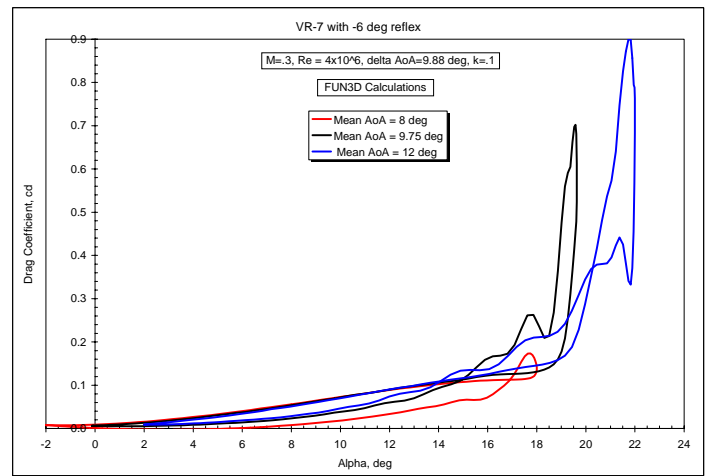
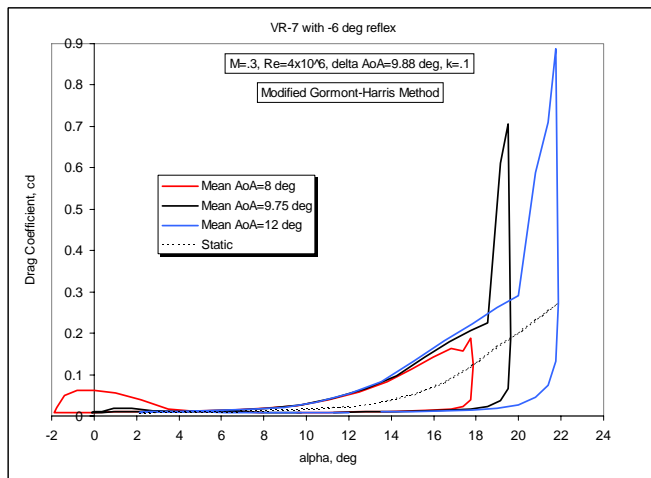
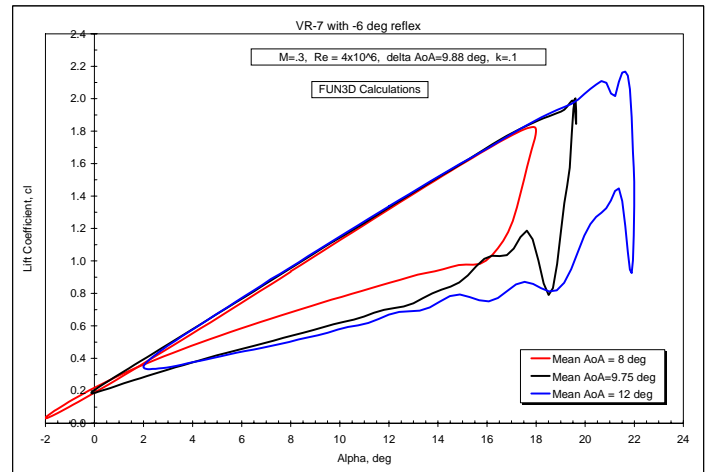
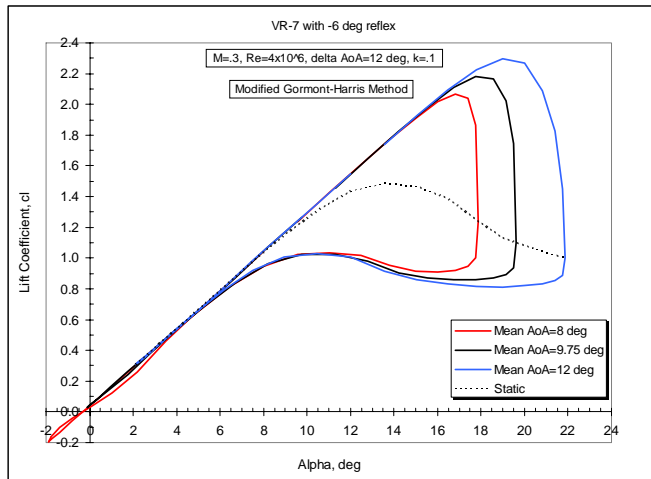


Figure 25 VR-7 dynamic stall characteristics as computed by empirical and CFD methods.

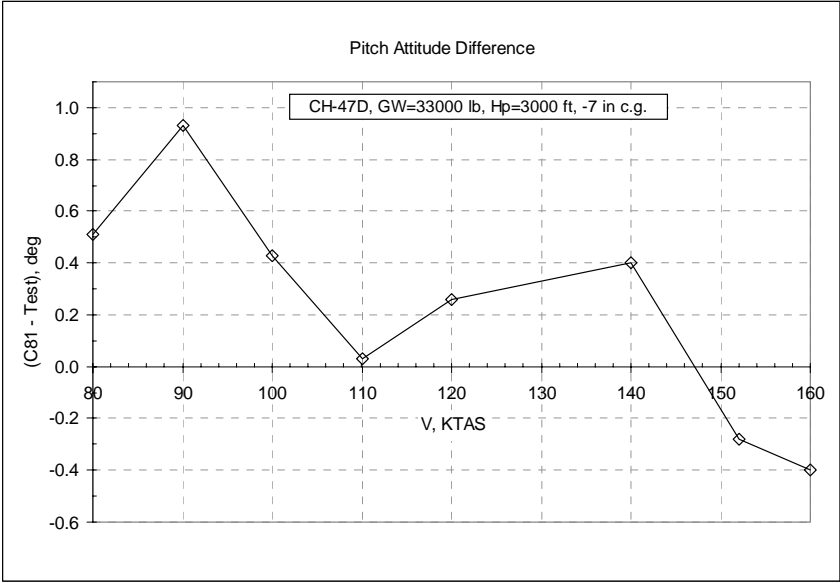


Figure 26 Difference in C81 calculated pitch angle and test.

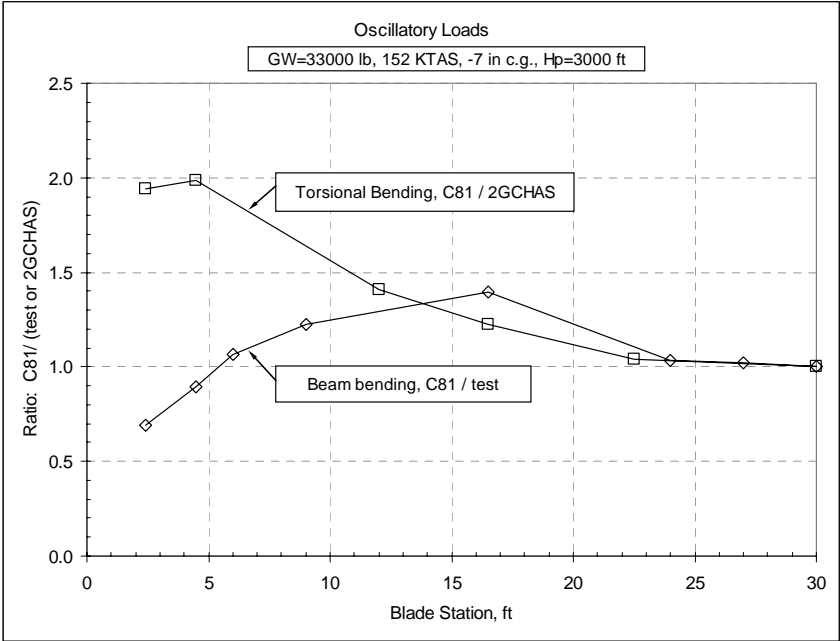


Figure 27 Ratio of C81 calculated loads to test and 2GCHAS.

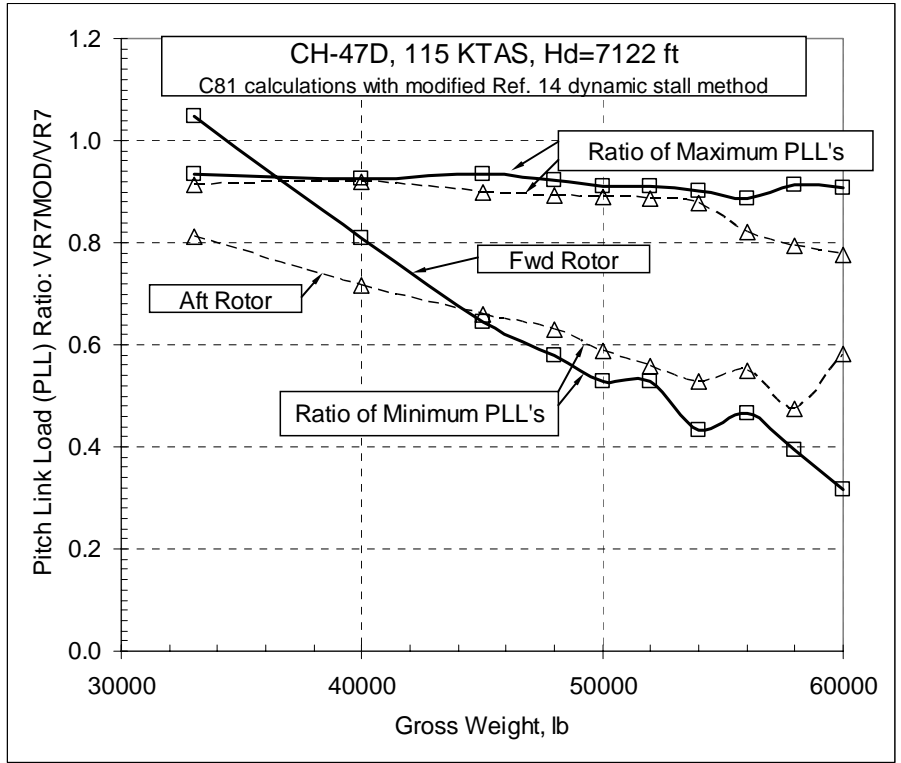


Figure 28 Calculated Pitch Link Load reduction at 115 KTAS due to airfoil modification.

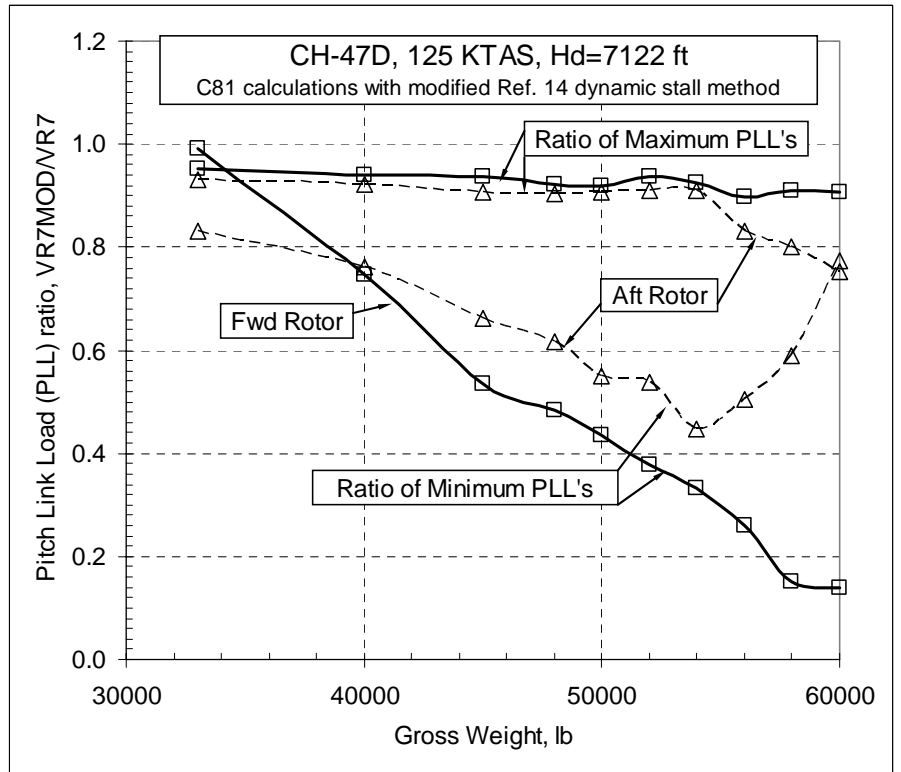
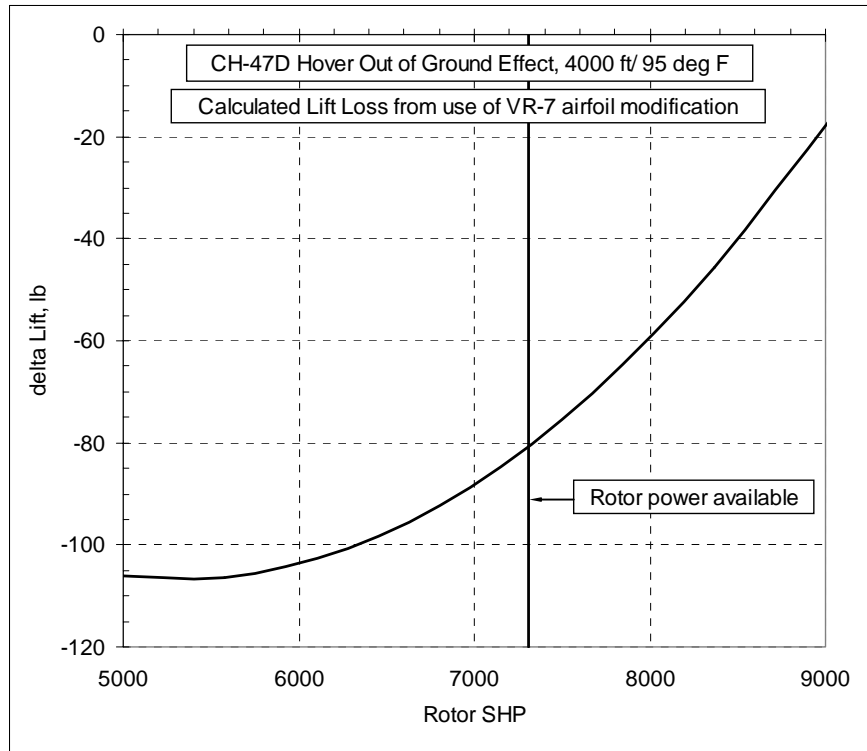


Figure 29 Calculated Pitch Link Load reduction at 125 KTAS due to airfoil modification.



**Figure 30 Calculated Lift loss at HOGE conditions due to use of modified VR-7 airfoil (optimized at  $M_{\infty}=0.3$ ) instead of standard VR-7 airfoil.**